



RESEARCH LETTER

10.1029/2018GL080137

Key Points:

- We provide detailed new observations that constrain variations in average creep rates following regional earthquakes
- A new model is proposed for understanding dynamic/static stress changes and short- and long-term creep rate variations on the shallow SSAF
- Our observations suggest that static stress change has a long-lasting effect on fault creep, even in the presence of transient processes

Supporting Information:

- Supporting Information S1

Correspondence to:

D. T. Sandwell,
dsandwell@ucsd.edu

Citation:

Xu, X., Ward, L., Jiang, J., Smith-Konter, B., Tymofyeyeva, E., Lindsey, E. O., et al. (2018). Surface creep rate of the southern San Andreas fault modulated by stress perturbations from nearby large events. *Geophysical Research Letters*, 45. <https://doi.org/10.1029/2018GL080137>

Received 21 AUG 2018

Accepted 24 AUG 2018

Accepted article online 29 AUG 2018

Surface Creep Rate of the Southern San Andreas Fault Modulated by Stress Perturbations From Nearby Large Events

Xiaohua Xu¹ , Lauren Ward², Junle Jiang^{1,3} , Bridget Smith-Konter² , Ekaterina Tymofyeyeva¹ , Eric O. Lindsey⁴ , Arthur G. Sylvester⁵, and David T. Sandwell¹

¹Institute of Geophysics and Planetary Physics, Scripps Institution of Oceanography, University of California, San Diego, La Jolla, CA, USA, ²Department of Geology and Geophysics, University of Hawai'i at Mānoa, Honolulu, HI, USA, ³Department of Earth and Atmospheric Sciences, Cornell University, Ithaca, NY, USA, ⁴Earth Observatory of Singapore, Nanyang Technological University, Singapore, ⁵Department of Earth Science, University of California, Santa Barbara, CA, USA

Abstract A major challenge for understanding the physics of shallow fault creep has been to observe and model the long-term effect of stress changes on creep rate. Here we investigate the surface creep along the southern San Andreas fault (SSAF) using data from interferometric synthetic aperture radar spanning over 25 years (ERS 1992–1999, ENVISAT 2003–2010, and Sentinel-1 2014–present). The main result of this analysis is that the average surface creep rate increased after the Landers event and then decreased by a factor of 2–7 over the past few decades. We consider quasi-static and dynamic Coulomb stress changes on the SSAF due to these three major events. From our analysis, the elevated creep rates after the Landers can only be explained by static stress changes, indicating that even in the presence of dynamically triggered creep, static stress changes may have a long-lasting effect on SSAF creep rates.

Plain Language Summary There are two significant conclusions from this study. First, we analyzed 25 years of InSAR measurements over the Southern San Andreas Fault system to document a major increase in the average creep rate following the 1992 Mw 7.3 Landers Earthquake which is then followed by creep rate reductions after the 1999 Mw 7.1 Hector Mine Earthquake and the 2010 Mw 7.2 El Major Cucapah Earthquake. Second, we attribute all these creep rate changes to the Coulomb stress variations from these three major Earthquakes. The dynamic Coulomb stress changes are similar for all three events, contributing to triggered creep on the SSAF. In contrast, the static Coulomb stress changes on the SSAF are positive after the Landers and negative after the Hector Mine and El Major Cucapah, coinciding with the higher average creep rate after the Landers and lower rates after the other two events. An implication of this study is that small but steady Coulomb stress changes have a larger impact on shallow creep than the larger dynamic stress changes associated with passing seismic waves. These results illuminate the significance of time scale-dependent complexity of shallow fault creep and how these behaviors are communicated by stress perturbations from regional earthquakes.

1. Introduction

Shallow fault creep is an aseismic faulting phenomenon observed on several active strike-slip faults (Bürgmann et al., 2000; Funning et al., 2007; Harris, 2017; Kaneko et al., 2013; Steinbrugge et al., 1960). The stable sliding of fault creep is generally governed by velocity-strengthening frictional properties, which is supported by both theoretical (Dieterich, 1978; Scholz, 1998; Tse & Rice, 1986) and experimental studies (Blanpied et al., 1995; Marone et al., 1991). Creep is driven by postseismic or interseismic stressing and can be continuous or episodic (Wesson, 1988). Creep rate is often observed to be high immediately following an earthquake and then diminishes with time after a few decades (Cakir et al., 2005; Wei et al., 2009). Triggered surface creep is commonly associated with dynamic or static stress changes from large nearby earthquakes and can be as large as a couple of centimeters (Behr et al., 1997; Kostić et al., 2014; Lienkaemper et al., 1997; Stein et al., 1992; Williams et al., 1988). Shallow creep also occurs during interseismic periods when there is no significant triggering, as a combination of steady creep punctuated by irregular creep events (Bilham et al., 2004).

Creep can be measured using various tools that sample differing space and time scales. Geologists can determine the average creep rate of a fault by measuring offsets of natural and man-made structures and

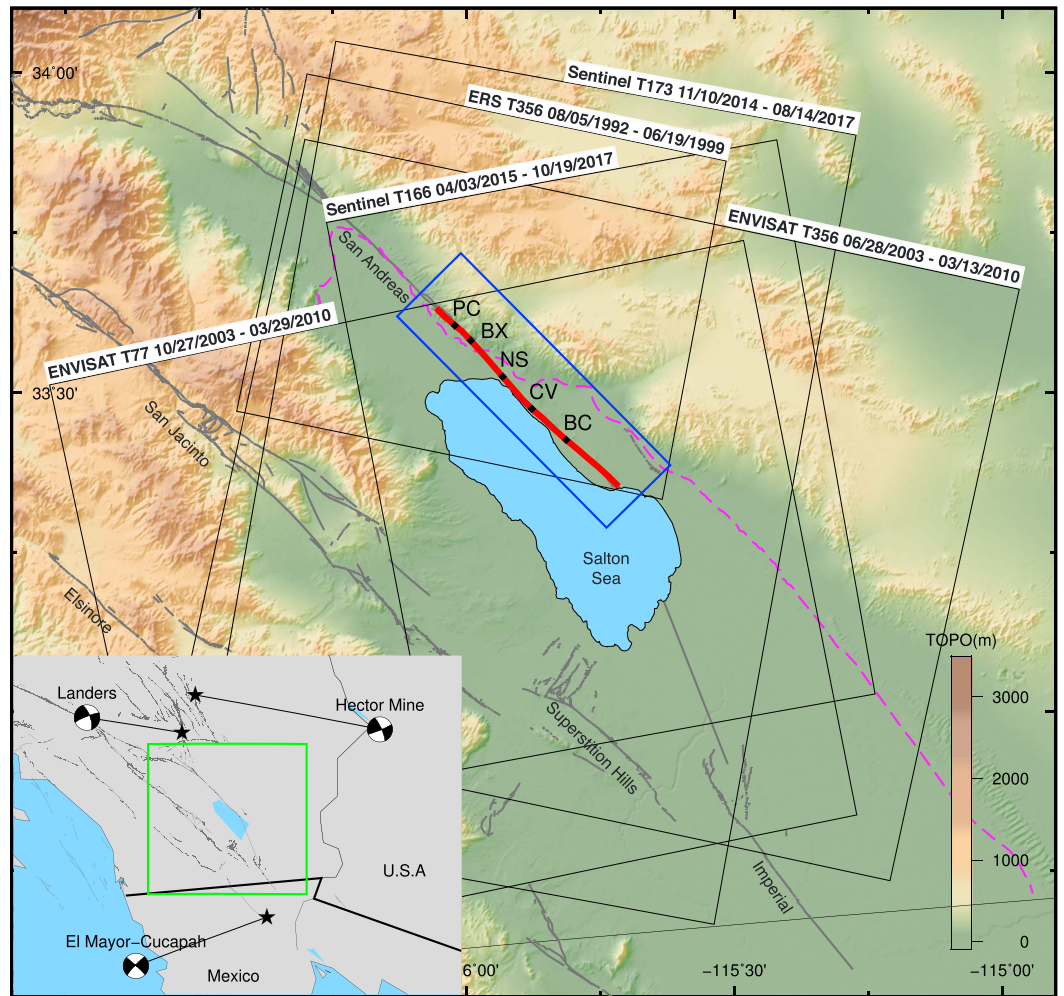


Figure 1. Southern San Andreas fault region. Creep rate is estimated at PC, BX, NS, CV, and BC. Outset map shows epicentral locations of the last three major earthquakes of the southern San Andreas fault region: 1992 M_w 7.3 Landers, 1999 M_w 7.1 Hector Mine, and 2010 M_w 7.2 El Mayor-Cucapah. PC = Painted Canyon; BX = Box Canyon; NS = North Shore; CV = Corvina Beach; BC = Bat Caves.

dating the duration of the creep period (Sieh & Williams, 1990). Creepmeters are highly accurate and provide a continuous record of creep but are spatially limited to a few meters on either side of a fault trace (Bilham et al., 2004). Alignment arrays can sample farther from the fault and thus capture more distributed shallow creep or creep on multiple fault traces, but their temporal resolution depends on how often the arrays are resurveyed (Louie et al., 1985). Interferometric synthetic aperture radar (InSAR) can provide a more complete mapping of distributed creep but is susceptible to atmospheric noises (Lyons & Sandwell, 2003). Thus, when examining InSAR, stacking or time series analysis is needed to resolve low creep rates less than ~ 5 mm/year, and the temporal resolution is usually limited by the cadence of SAR acquisitions.

The reported creep rates along the southern San Andreas fault (SSAF; Figure 1) are somewhat variable depending on the location as well as the spatial and temporal scales of the observations (Table 1). Over the past 300 years, the average geologic creep rates near Indio and the Salton Sea are estimated to be 2–4 mm/year (Sieh & Williams, 1990). Creep in the same region for the time period of 1970 to 1984, derived from alignment arrays and creepmeters, is generally less than 2 mm/year (Louie et al., 1985). Similar creepmeter rates were found for the time period 1968–1979 (Bilham & Williams, 1985). More recent ERS InSAR measurements of creep rates for the time period between the 1992 Landers and 1999 Hector Mine earthquakes are generally significantly higher (Lyons & Sandwell, 2003; 0–6 mm/year from Painted Canyon [PC] to Box Canyon [BX], 15–20 mm/year from North Shore [NS] to Corvina Beach [CV]). The mismatch among these

Table 1
Creep Rate Estimates (mm/year)

	Time span	PC	BX	NS	CV	BC
Sieh and Williams (1990)	Past 300 years	2–4	2–4	-	4 ^a	4 ^b
Louie et al. (1985)	~1970–1984	2.0	3.1	0.08	0.7	1–2
Lyons and Sandwell (2003) ^c	1992/08–1999/06	0–6	0–6	15–20	15–20	-
Tong et al. (2013) ^d	2006/06–2010/12	4–5	3–5	3–5	4–5	0
Lindsey et al. (2014)	2003/06–2010/10	2.7	2.2	2.6	4.5	3.0
ERS (this study)	1992/08–1999/06	2.6	3.7	1.9	7.5	3.3
ENVISAT (this study)	2003/06–2010/03	2.4	2.0	1.0	4.2	2.4
Sentinel-1 (this study)	2014/11–present	1.7	0.4	0.0	1.6	1.9

Note. PC = Painted Canyon; BX = Box Canyon; NS = North Shore; CV = Corvina Beach; BC = Bat Caves.

^aAverage creepmeter rate at Mecca Beach 2-km north to BC from 1981 to 1988 is ~4 mm/year. ^bAverage creep rate at Ferrum 4-km north to BC for 297 years is 4.0 ± 1.0 mm/year. ^cThese values are visual estimates from single look direction, fault-crossing profiles and include signal from deep slip. ^dThese values were estimated from a single look direction.

higher modern values from InSAR observations and the prior lower values could be errors caused by scaling the single line of sight (LOS) measurements from ERS into horizontal strike-slip motion without accounting for vertical signals across the fault (Sylvester et al., 1993). A more recent InSAR analysis (Lindsey et al., 2014) using two look directions of ENVISAT data spanning 2003 to 2010 showed smaller creep rates than found in the ERS study (i.e., at the five locations shown in Figure 1, PC = 2.7 mm/year, BX = 2.2 mm/year, NS = 2.6 mm/year, CV = 4.5 mm/year, and Bat Caves (BC) = 3.0 mm/year). Moreover, these values agree with creepmeter measurements (Bilham et al., 2004) over the same time period except for NS, where the surface creep is distributed over 1.5 km across the fault. Similar estimates of 3–5 mm/year were deduced by studies using only one look direction of ALOS-1 data spanning between 2006 and 2010 (Tong et al., 2013). The discrepancies among these studies raise two questions. First, are the creep rates really changing over decadal time scales? Second, if so, what are the possible physical mechanisms that could explain this change?

To address the first question, we reprocessed InSAR data from five satellites (ERS-1/2, ENVISAT, Sentinel-1A/B) that cover the SSAF area with a total observational period spanning over 25 years. We selected interferograms that do not span the times of the nearby major earthquakes (e.g., Landers, Hector Mine, and El Major-Cucapah [EMC]), thus the estimated surface creep rate should not have a significant triggered component. We then extracted creep rate profiles along the SSAF trace and computed the fault parallel component either by combining measurements from two radar look directions or calibrating the measurement from one radar look direction using leveling data (Sylvester et al., 1993). The Sentinel-1 analysis (2014–present) provides a third decade of creep rate measurements to compare with the ERS (1990s) and ENVISAT (2000s) decades (supporting information Figure S1); surprisingly, we find that the present-day creep rates are lower than all the previous studies discussed above and thus confirm that temporal variations are real. To begin to explain these temporal variations in creep rate, we calculate Coulomb stress changes on the SSAF due to regional large earthquake events using detailed source models (Xu et al., 2016) and explore possible explanations for observations in models of stress interactions on friction-controlled faults.

2. InSAR Velocity Analyses

The InSAR processing and creep rate estimation was done using GMTSAR (Sandwell et al., 2011; Wessel et al., 2013) and largely followed workflows of Lindsey et al. (2014) and Xu et al. (2017; Text S1). The interferograms were Gaussian filtered at 100-m wavelength and then unwrapped with SNAPHU (Chen & Zebker, 2002). Tropospheric error was reduced by stacking (Fialko, 2006; Peltzer et al., 2001) combined with an elevation-dependent correction (Elliott et al., 2008). Residual long-wavelength errors were corrected using a GPS velocity model (Sandwell & Wessel, 2016; Tong et al., 2013; Wei et al., 2010). When multiple look directions were available, we decomposed the LOS velocities into vertical (Figure S4) and fault parallel (Figure 2, top panel) directions. Creep rate and uncertainty were estimated by linearly regressing the data in 2- (fault-perpendicular) by 4-km (fault-parallel) boxes (Figure 2, top panel). Since the ERS data have only one look direction, we

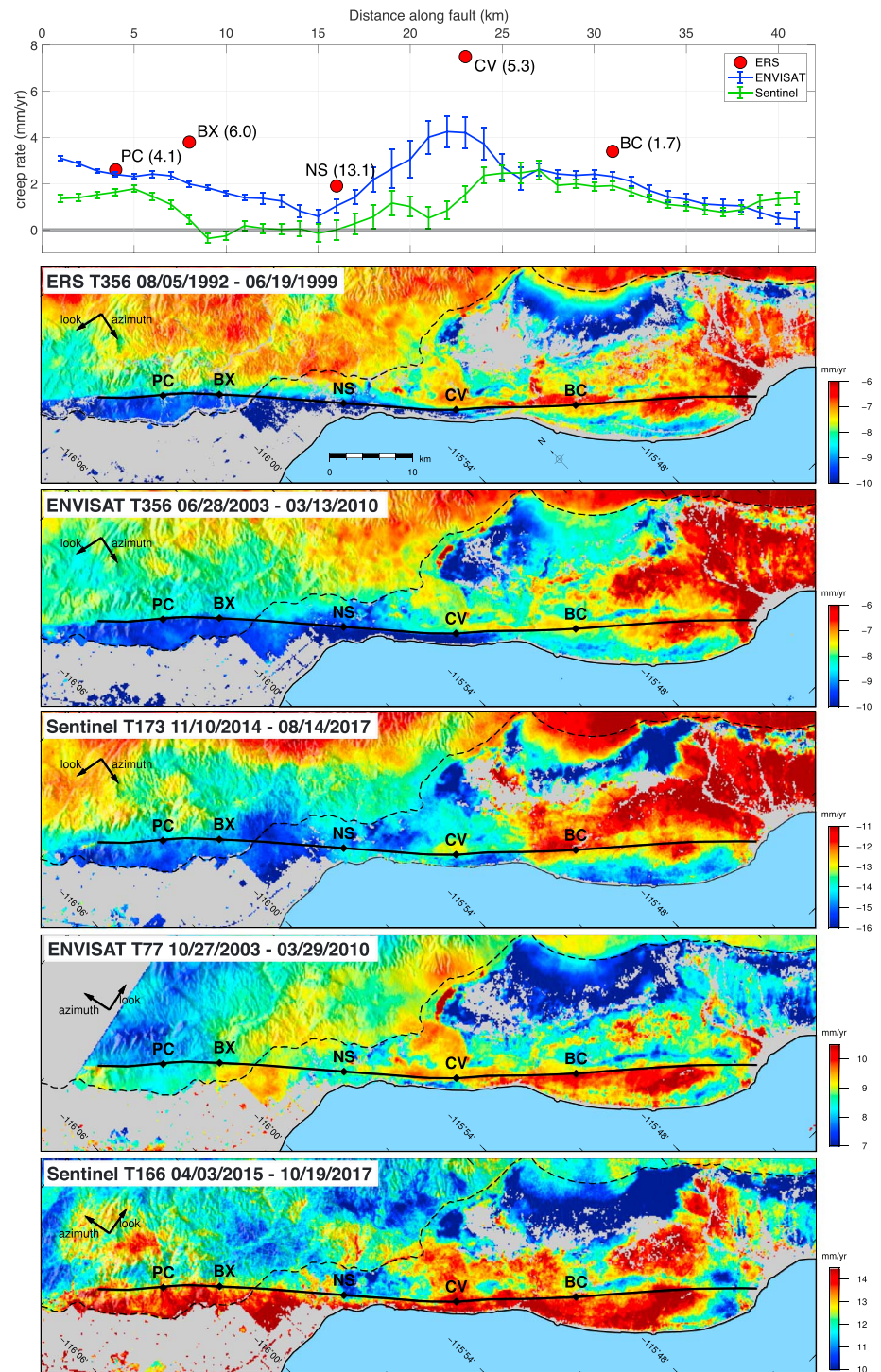


Figure 2. Line of sight velocity and creep rate. (upper) Fault-parallel creep rate where red circles are ERS-creep velocities corrected for vertical deformation (uncorrected in parentheses). The creep rate uncertainties are computed via linear regression on the interferometric synthetic aperture radar profiles and then propagated through decomposition. (lower) Interferometric synthetic aperture radar line of sight velocity with red toward satellite. The dashed line is the Coachella Canal and arrows show satellite flight and look directions. PC = Painted Canyon; BX = Box Canyon; NS = North Shore; CV = Corvina Beach; BC = Bat Caves.

first projected the vertical leveling measurements that are available at five positions (PC, BX, NS, CV, and BC) along this segment (Figures S2 and S4; Sylvester et al., 1993) into the descending LOS direction. Then we subtracted these from the InSAR measurements (Figure S3) and projected the results back to the fault-parallel direction.

3. Temporal Variations in Creep Rate

We observe (Figure 2) a major decrease in creep rate by a factor of about 2 to 7 between the ERS time frame and the present (Sentinel time frame). The smallest reduction was at PC where creep rate was 2.6 mm/year during the ERS time frame, 2.4 mm/year during the ENVISAT time frame, and 1.7 mm/year today. CV had the largest creep rate reduction from 7.5 (ERS) to 4.2 (ENVISAT) to 1.6 mm/year (Sentinel) today. The BX creep rates varied from 3.7 to 2.0 to 0.4 mm/year. The most important observation comes from Sentinel-1, where we see very little to almost no long-term average creep today on the SSAF.

This reanalysis of the ENVISAT data agrees well with the analysis of Lindsey et al. (2014); small differences can be attributed to the omission of interferograms that span the 2010 EMC earthquake. The reanalysis of the ERS data yields generally lower LOS creep rates (Figure 2) than the Lyons and Sandwell (2003) study which did not account for vertical motions across the fault. The largest difference is at NS where the vertical velocity from the leveling data (Sylvester et al., 1993) reduces the creep rate from 13.1 to about 2 mm/year (Figure 2, top panel). The other adjustments are significantly smaller. One possible explanation for this large vertical velocity at NS is that it represents tectonic motion due to the more westerly strike of this segment (Lindsey et al., 2014). A second possible explanation is that groundwater leaking from an unlined section of the Coachella Valley Canal (dashed lines in LOS images) causes ground deformation and swelling. NS is close enough to the unlined canal to have significant vertical deformation across the SSAF. This entire section of canal was concrete lined in 2006, which would have reduced the ground swelling and the vertical deformation for the ENVISAT and Sentinel-1 analyses. Therefore, we consider that the creep rate at NS during the ERS time frame is largely uncertain, whereas the others are more reliable. We note that the creep at CV is well resolved in all three InSAR analyses, and it has the greatest reduction from 7.5 to 1.6 mm/year. To begin to understand the cause of this dramatic reduction, we have investigated the change in static stress rate over this 25-year period caused by nearby major earthquakes.

4. Coulomb Stress Changes by Nearby Earthquakes

Time-dependent Coulomb stress changes (King et al., 1994) due to the three major earthquakes were calculated using a viscoelastic model (Smith & Sandwell, 2004; plate thickness 60 km, a Young's modulus 70 GPa, shear modulus of 30 GPa, mantle viscosity of 1×10^{19} Pa/s, and coefficient of friction of 0.6). Coseismic slip models from Xu et al. (2016) were used to calculate quasi-static stress changes associated with each earthquake (Figures 3a–3c), as well as the postseismic stress relaxation in the years that follow (Figure 3e). Note that interseismic background stressing rates along the SSAF segment and nearby faults (~ 20 – 30 kPa/year; Smith-Konter & Sandwell, 2009) are not included. Coulomb stress on the receiver fault was calculated at 1 km depth (Figure 3, lower). Step changes in stress are due to the earthquakes, whereas the more gradual changes are due to viscoelastic relaxation. Resolved shear and normal components are also provided in Figures S5–S6. We note that an elastic half-space model (Stein et al., 1992; Toda et al., 2005) gives the same coseismic stress change but with no stress evolution between events.

5. Is Creep Rate Modulated by Dynamic or Static Stress Changes?

First, we consider the effects of dynamic, and static stress changes explain the observed temporal variations in creep rate. Dynamic triggering occurs when stresses from passing seismic waves cause near-instantaneous creep that is followed by a decrease in creep rate for a few months (Rymer et al., 2002; Wei et al., 2011). The three large nearby earthquakes produced dynamic stress variations of ~ 500 kPa (Figures S7 and S8) which are about 40 times larger than the peak static Coulomb stress change following the Landers event. However, these imposed stress changes are short-lived and vanish within minutes. Instantaneously dynamically triggered creep would lead to reduced creep rates after the earthquakes, but we see both increase and decrease in creep rates following the Landers and the Hector Mine/EMC events, respectively. Therefore, the temporal variations in long-term creep rates cannot be explained by dynamic triggering alone.

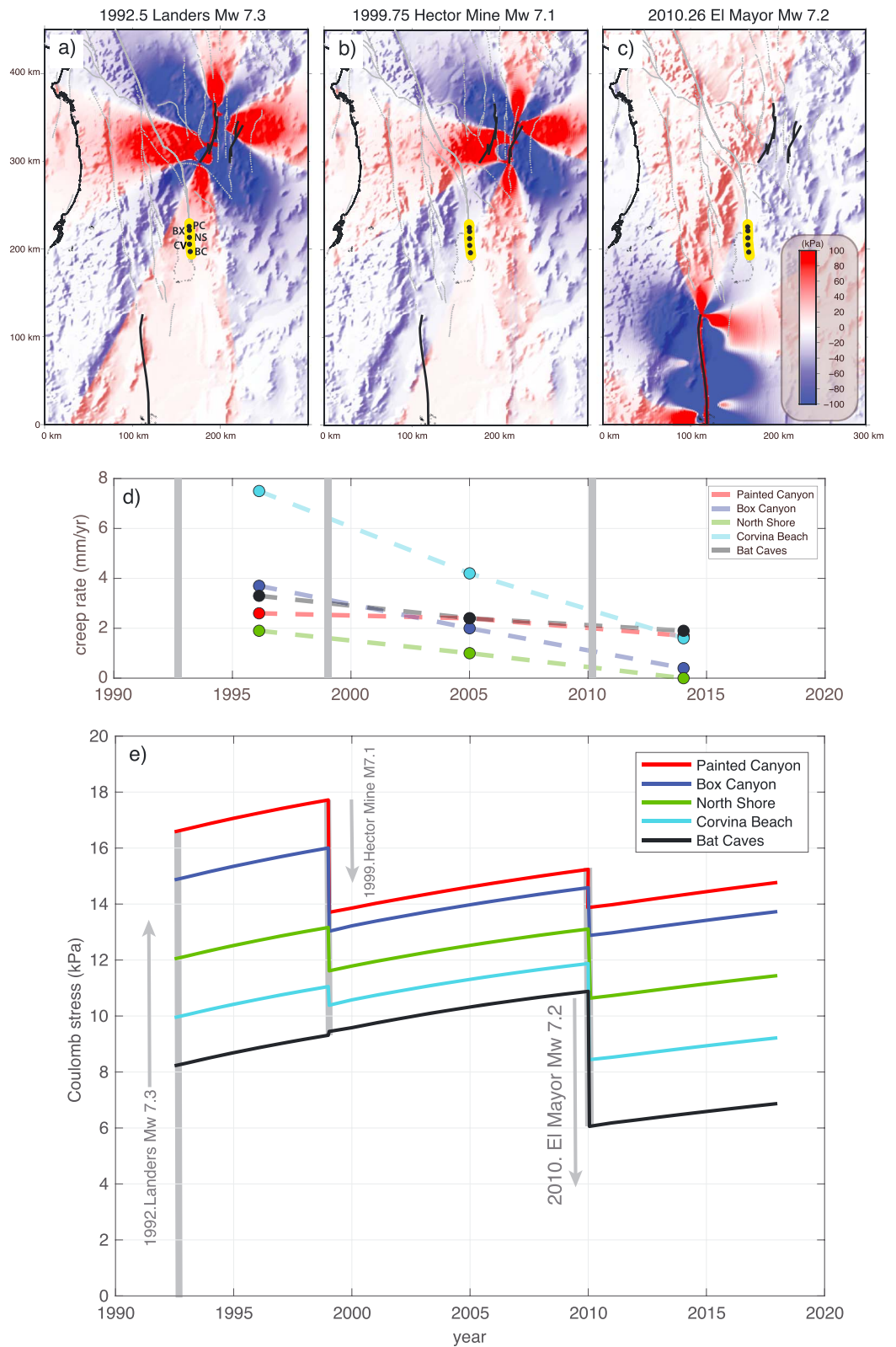


Figure 3. Coulomb stress change in response to the (a) Landers, (b) Hector Mine, and (c) El Mayor-Cucapah earthquakes in southern California. (d) Creep rates decrease systematically with time at the five locations with leveling data. (e) Coulomb stress versus time at the five locations has a large increase from the Landers earthquake and smaller decreases from Hector Mine and El Mayor-Cucapah. PC = Painted Canyon; BX = Box Canyon; NS = North Shore; CV = Corvina Beach; BC = Bat Caves.

A second type of dynamic triggering occurs because of a change in fault zone permeability due to dynamic stresses from passing seismic waves (Elkhoury et al., 2006), which could affect the pore-fluid pressure, the effective normal stress, and thereby the creep rate. However, the variation in permeability occurs over time periods of a few months and, like dynamic triggering, its influence on creep rate always has the same sign and is unable to explain our observations.

We suggest that the smaller yet permanent change in static Coulomb stress plays a dominant role in modulating long-term creep rates, because it can explain both increases and decreases in creep rate. From our calculations, the largest overall static stress change was caused by the 1992 Landers earthquake, which produced a stress increase of 8–16.5 kPa at the five sites (Figure 3). The largest stress increase occurred at PC, which is closest to the Landers rupture (~75 km away). Stresses increase slightly for the 7 years following the Landers event due to viscoelastic rebound. The 1999 Hector Mine rupture produced a 0.5–4 kPa stress drop at four of the five sites; BC experienced a very small stress increase (<0.25 kPa) due to its position with respect to Hector Mine's positive southern stress change lobe. Postseismic stress variations following the Hector Mine earthquake were largely dominated by the continuing Landers (positive) relaxation signal. The April 2010 EMC rupture produced a 1.3–5 kPa stress drop at all five sites, with the largest stress drop at BC, which is closest to the northern limit of the El Mayor rupture. Postseismic stress change following the EMC earthquake is dominated by the Landers relaxation signal.

Temporal variations in creep rate (Figure 2) are somewhat correlated with these Coulomb stress changes (Figure 3). Prior to the 1992 Landers earthquake, typical creep rates on the SSAF were relatively low at ~2–4 mm/year (Louie et al., 1985; Sieh & Williams, 1990). The higher creep rates on the SSAF following the Landers earthquake and the later lower values following the Hector Mine and EMC earthquakes coincide with positive and negative stress changes, respectively.

This correlation between the static stress change and fault slip rate can be understood in the framework of rate-and-state fault friction. For stable, velocity-strengthening fault frictional properties that are typically used to describe shallow faults, a positive Coulomb stress change causes an instantaneous increase in creep rate, with time-dependent relaxation ensuing; a negative stress change causes an immediate decrease of creep rates (e.g., Perfettini & Avouac, 2004). Using a 1-D fault model with parameters motivated by the SSAF, we demonstrate that a step increase/decrease of Coulomb stress on the order of ~20 kPa can plausibly result in a multiyear increase/decrease of fault creep rates (Text S2; Figures S9 and S10). This model would also predict that the creep rate would decrease during the decade following the ERS event. To test this decrease, we split the ERS stack at June 1996 and computed two rates (1992–1996, 1996–1999). We find that, indeed, there is a significant decrease in rate between the two periods (Figure S3), although the creep rate uncertainties are much larger when the timespan is bisected.

We note that this long-term modulation of the creep rate by Coulomb stress changes is similar to the long-term evolution in seismicity rate following the Landers and Hector Mine earthquakes (Toda et al., 2005). They find that positive Coulomb stress changes amplify the background seismicity, whereas negative stress changes suppress the background seismicity, over time scales of years to decades, similar to our observed correlations. The effect of static stress changes on creep rates also resemble those in postseismic studies of afterslip surrounding earthquake-ruptured region on the fault (e.g., Marone et al., 1991), although the involved stress/rate changes here have much smaller amplitudes.

Compared to aftershock or afterslip processes, triggered creep on the SSAF is characterized by both transient and long-term changes in fault stress and slip rate. While the existence of fault creep above the seismogenic zone is readily explained by velocity-strengthening frictional properties of the near-surface fault zone, transient creep events are well-documented on some fault areas immediately following regional earthquakes, suggesting that other physical mechanisms are involved, such as conditionally stable frictional properties (e.g., Liu & Rice, 2005; Wei et al., 2013), geometrical complexities (e.g., Romanet et al., 2018), or pore pressure variations (e.g., Khoshmanesh & Shirzaei, 2018; Segall & Rice, 1995).

To aid the interpretation of observations, we summarize the creep triggering processes on the SSAF in a conceptual model (Figure 4). The regional earthquake can dynamically trigger creep in some fault areas, leading to a reduced long-term creep rate while imparting stress changes to nearby fault areas. Consequently, the static stress perturbations on fault areas that accommodate steady creep, due to both the earthquake and local triggered creep, modulate the creep rates over the long term. Our InSAR

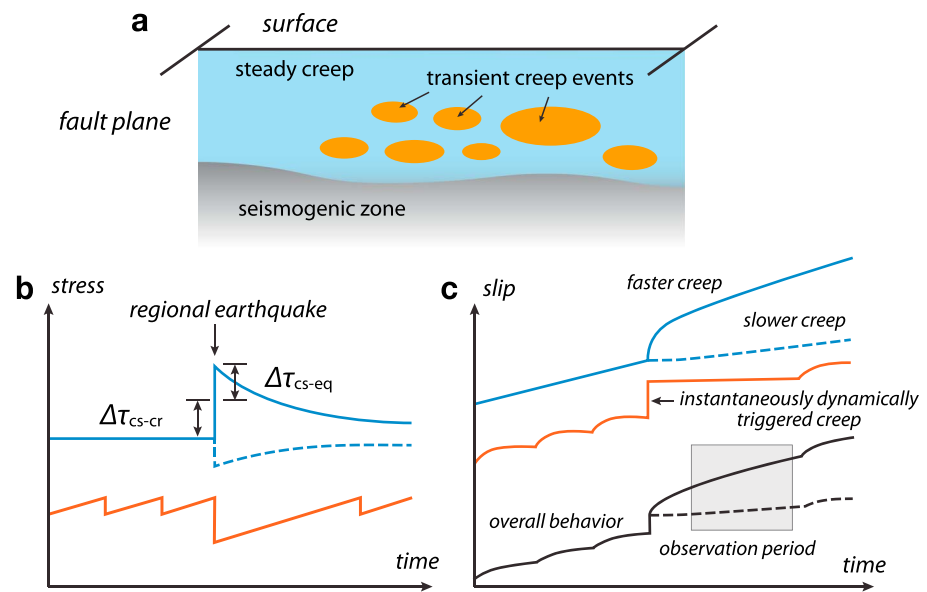


Figure 4. A conceptual model for creep triggering on the shallow southern San Andreas fault. (a) The shallow fault zone consists of areas that accommodate steady creep (blue) and host transient creep events triggered by nearby earthquakes (orange). Time evolution of stress and slip within the two types of fault areas are illustrated in (b) and (c), respectively. In fault areas with steady creep, regional earthquakes produce static stress change $\Delta\tau_{cs-eq}$; dynamically triggered creep events produce additional stress change $\Delta\tau_{cs-cr}$ (solid and dashed lines for cases with positive and negative stress changes). The overall creep rate for the shallow fault zone is shown in black curves.

observations constrain the overall creep rates of the shallow SSAF, including fault areas with both creep modes. Note that such stress transfer processes and collective kinematic behavior should hold regardless of the underlying mechanisms for different creep behavior. While a postevent decrease in the average creep rate may be attributed to either dynamic or static stress shadow effect, a much higher postevent creep rate, as observed after the Landers, can only be explained by static stress change.

6. Conclusions

Recent observation from Sentinel-1 of anomalously low creep rate on the SSAF has prompted a complete reanalysis of 25 years of InSAR data to examine spatial and temporal variations in creep rate. We see a considerable increase in average creep rate after the 1992 Landers earthquake and a 2–7 times decrease in creep rate from the ERS time frame to the present. We calculate the Coulomb stress changes associated with the major earthquakes surrounding the SSAF and consider interactions between quasi-static and dynamic processes and their implications for the observed fault creep behavior. While dynamically triggered creep is well documented on the SSAF, the average fault creep rates, in particular the elevated rates after the Landers, are best explained by the long-term effect of static Coulomb stress changes. Analysis of space- and land-based geodetic techniques over the next decades will enable a further refinement of these variations on time scales ranging from days to decades. The current observations of fault creep rate and inferred stress transfer processes, with more examples from future regional events, will provide critical test cases for understanding near-surface fault zone conditions and multitime scale dynamics of fault creep.

References

- Behr, J., Bilham, R., Bodin, P., Breckenridge, K., & Sylvester, A. G. (1997). Increased surface creep rates on the San Andreas fault southeast of the Loma Prieta mainshock, pp. D179-D192, in Reasonberg, P., editor, *The Loma Prieta, California, Earthquake of October 17, 1989 — Aftershocks and Postseismic Effects*. U.S. Geological Survey Professional Paper 1550-D, 312 p.
- Bilham, R., Suszek, N., & Pinkney, S. (2004). California creepmeters. *Seismological Research Letters*, 75(4), 481–492. <https://doi.org/10.1785/gssrl.75.4.481>
- Bilham, R., & Williams, P. (1985). Sawtooth segmentation and deformation processes on the southern San Andreas fault, California. *Geophysical Research Letters*, 12(9), 557–560. <https://doi.org/10.1029/GL012i009p00557>

Acknowledgments

The authors thank ESA for the extraordinary open policy on all the data sets and thank ASF and UNAVCO for archiving the data and orbital products. The fault traces were provided by USGS and CICESE. This study was funded by the NASA Earth Surface and Interior Program (NNX16AK93G), the National Science Foundation (EAR-1614875), and the Southern California Earthquake Center (SCEC; Award numbers 17042 and 16177). SCEC is funded by the NSF cooperative Agreement EAR-1033462 and USGS Cooperative Agreement G12AC20038.

- Blanpied, M. L., Lockner, D. A., & Byerlee, J. D. (1995). Frictional slip of granite at hydrothermal conditions. *Journal of Geophysical Research*, 100(B7), 13,045–13,064. <https://doi.org/10.1029/95JB00862>
- Bürgmann, R., Schmidt, D., Nadeau, R. M., d'Alessio, M., Fielding, E., Manaker, D., & Murray, M. H. (2000). Earthquake potential along the northern Hayward fault, California. *Science*, 289(5482), 1178–1182. <https://doi.org/10.1126/science.289.5482.1178>
- Cakir, Z., Akoglu, A. M., Belabbes, S., Ergintav, S., & Meghraoui, M. (2005). Creeping along the Ismetpasa section of the North Anatolian fault (Western Turkey): Rate and extent from InSAR. *Earth and Planetary Science Letters*, 238(1–2), 225–234. <https://doi.org/10.1016/j.epsl.2005.06.044>
- Chen, C. W., & Zebker, H. A. (2002). Phase unwrapping for large SAR interferograms: Statistical segmentation and generalized network models. *IEEE Transactions on Geoscience and Remote Sensing*, 40(8), 1709–1719. <https://doi.org/10.1109/TGRS.2002.802453>
- Dieterich, J. H. (1978). Time-dependent friction and the mechanics of stick-slip. In *Rock Friction and Earthquake Prediction* (pp. 790–806). Birkhäuser, Basel.
- Elkhoury, J. E., Brodsky, E. E., & Agnew, D. C. (2006). Seismic waves increase permeability. *Nature*, 441(7097), 1135–1138. <https://doi.org/10.1038/nature04798>
- Elliott, J. R., Biggs, J., Parsons, B., & Wright, T. J. (2008). InSAR slip rate determination on the Altyn Tagh fault, northern Tibet, in the presence of topographically correlated atmospheric delays. *Geophysical Research Letters*, 35, L12309. <https://doi.org/10.1029/2008GL033659>
- Fialko, Y. (2006). Interseismic strain accumulation and the earthquake potential on the southern San Andreas fault system. *Nature*, 441(7096), 968–971. <https://doi.org/10.1038/nature04797>
- Funning, G. J., Bürgmann, R., Ferretti, A., Novali, F., & Fumagalli, A. (2007). Creep on the Rodgers Creek fault, northern San Francisco Bay area from a 10-year PS-InSAR dataset. *Geophysical Research Letters*, 34, L19306. <https://doi.org/10.1029/2007GL030836>
- Harris, R. A. (2017). Large earthquakes and creeping faults. *Reviews of Geophysics*, 55, 169–198. <https://doi.org/10.1002/2016RG000539>
- Kaneko, Y., Fialko, Y., Sandwell, D. T., Tong, X., & Furuya, M. (2013). Interseismic deformation and creep along the central section of the North Anatolian fault (Turkey): InSAR observations and implications for rate-and-state friction properties. *Journal of Geophysical Research: Solid Earth*, 118, 316–331. <https://doi.org/10.1029/2012JB009661>
- Khoshranesh, M., & Shirzaei, M. (2018). Episodic creep events on the San Andreas fault caused by pore pressure variations. *Nature Geoscience*, 11(8), 610–614. <https://doi.org/10.1038/s41561-018-0160-2>
- King, G. C., Stein, R. S., & Lin, J. (1994). Static stress changes and the triggering of earthquakes. *Bulletin of the Seismological Society of America*, 84(3), 935–953.
- Kostić, S., Franović, I., Perc, M., Vasović, N., & Todorović, K. (2014). Triggered dynamics in a model of different fault creep regimes. *Scientific Reports*, 4(1), 5401. <https://doi.org/10.1038/srep05401>
- Lienkaemper, J. J., Galehouse, J. S., & Simpson, R. W. (1997). Creep response of the Hayward fault to stress changes caused by the Loma Prieta earthquake. *Science*, 276(5321), 2014–2016. <https://doi.org/10.1126/science.276.5321.2014>
- Lindsey, E. O., Fialko, Y., Bock, Y., Sandwell, D. T., & Bilham, R. (2014). Localized and distributed creep along the southern San Andreas fault. *Journal of Geophysical Research: Solid Earth*, 119, 7909–7922. <https://doi.org/10.1002/2014JB011275>
- Liu, Y., & Rice, J. R. (2005). Aseismic slip transients emerge spontaneously in three-dimensional rate and state modeling of subduction earthquake sequences. *Journal of Geophysical Research*, 110, B08307. <https://doi.org/10.1029/2004JB003424>
- Louie, J. N., Allen, C. R., Johnson, D. C., Haase, P. C., & Cohn, S. N. (1985). Fault slip in southern California. *Bulletin of the Seismological Society of America*, 75(3), 811–833.
- Lyons, S., & Sandwell, D. (2003). Fault creep along the southern San Andreas from interferometric synthetic aperture radar, permanent scatterers, and stacking. *Journal of Geophysical Research*, 108(B1), 2047. <https://doi.org/10.1029/2002JB001831>
- Marone, C. J., Scholz, C. H., & Bilham, R. (1991). On the mechanics of earthquake afterslip. *Journal of Geophysical Research*, 96(B5), 8441–8452. <https://doi.org/10.1029/91JB00275>
- Peltzer, G., Crampé, F., Hensley, S., & Rosen, P. (2001). Transient strain accumulation and fault interaction in the eastern California shear zone. *Geology*, 29(11), 975–978. [https://doi.org/10.1130/0091-7613\(2001\)029<0975:TSAFI>2.0.CO;2](https://doi.org/10.1130/0091-7613(2001)029<0975:TSAFI>2.0.CO;2)
- Perfettini, H., & Avouac, J.-P. (2004). Postseismic relaxation driven by brittle creep: A possible mechanism to reconcile geodetic measurements and the decay rate of aftershocks, application to the Chi-Chi earthquake, Taiwan. *Journal of Geophysical Research*, 109, B02304. <https://doi.org/10.1029/2003JB002488>
- Romanet, P., Bhat, H. S., Jolivet, R., & Madariaga, R. (2018). Fast and slow slip events emerge due to fault geometrical complexity. *Geophysical Research Letters*, 45(10), 4809–4819. <https://doi.org/10.1029/2018GL077579>
- Rymer, M. J., Boatwright, J., Seekins, L. C., Yule, J. D., & Liu, J. (2002). Triggered surface slips in the Salton Trough associated with the 1999 Hector Mine, California, earthquake. *Bulletin of the Seismological Society of America*, 92(4), 1300–1317. <https://doi.org/10.1785/0120000935>
- Sandwell, D., Mellors, R., Tong, X., Wei, M., & Wessel, P. (2011). Open radar interferometry software for mapping surface deformation. *Eos, Transactions American Geophysical Union*, 92(28), 234–234. <https://doi.org/10.1029/2011EO280002>
- Sandwell, D. T., & Wessel, P. (2016). Interpolation of 2-D vector data using constraints from elasticity. *Geophysical Research Letters*, 43, 10,703–10,709. <https://doi.org/10.1002/2016GL070340>
- Scholz, C. H. (1998). Earthquakes and friction laws. *Nature*, 391(6662), 37–42. <https://doi.org/10.1038/34097>
- Segall, P., & Rice, J. R. (1995). Dilatancy, compaction, and slip instability of a fluid-infiltrated fault. *Journal of Geophysical Research*, 100(B11), 22,155–22,171. <https://doi.org/10.1029/95JB02403>
- Sieh, K. E., & Williams, P. L. (1990). Behavior of the southernmost San Andreas fault during the past 300 years. *Journal of Geophysical Research*, 95(B5), 6629–6645. <https://doi.org/10.1029/JB095iB05p06629>
- Smith, B., & Sandwell, D. (2004). A three-dimensional semianalytic viscoelastic model for time-dependent analyses of the earthquake cycle. *Journal of Geophysical Research*, 109, B12401. <https://doi.org/10.1029/2004JB003185>
- Smith-Konter, B., & Sandwell, D. (2009). Stress evolution of the San Andreas fault system: Recurrence interval versus locking depth. *Geophysical Research Letters*, 36, L13304. <https://doi.org/10.1029/2009GL037235>
- Stein, R. S., King, G. C., & Lin, J. (1992). Change in failure stress on the southern San Andreas fault system caused by the 1992 magnitude = 7.4 Landers earthquake. *Science*, 258(5086), 1328–1332. <https://doi.org/10.1126/science.258.5086.1328>
- Steinbrugge, K. V., Zacher, E. G., Tocher, D., Whitten, C. A., & Claire, C. N. (1960). Creep on the San Andreas fault. *Bulletin of the Seismological Society of America*, 50(3), 389–415.
- Sylvester, A. G., Bilham, R., Jackson, M., & Barrientos, S. (1993). Aseismic growth of Durmid Hill, southeasternmost San Andreas fault, California. *Journal of Geophysical Research*, 98(B8), 14,233–14,243. <https://doi.org/10.1029/93JB01028>
- Toda, S., Stein, R. S., Richards-Dinger, K., & Bozkurt, S. B. (2005). Forecasting the evolution of seismicity in southern California: Animations built on earthquake stress transfer. *Journal of Geophysical Research*, 110, B05S16. <https://doi.org/10.1029/2004JB003415>
- Tong, X., Sandwell, D. T., & Smith-Konter, B. (2013). High-resolution interseismic velocity data along the San Andreas fault from GPS and InSAR. *Journal of Geophysical Research: Solid Earth*, 118, 369–389. <https://doi.org/10.1029/2012JB009442>

- Tse, S. T., & Rice, J. R. (1986). Crustal earthquake instability in relation to the depth variation of frictional slip properties. *Journal of Geophysical Research*, 91(B9), 9452–9472. <https://doi.org/10.1029/JB091iB09p09452>
- Tymofyeyeva, E., & Fialko, Y. (2015). Mitigation of atmospheric phase delays in InSAR data, with application to the eastern California shear zone. *Journal of Geophysical Research: Solid Earth*, 120, 5952–5963. <https://doi.org/10.1002/2015JB011886>
- Wei, M., Kaneko, Y., Liu, Y., & McGuire, J. J. (2013). Episodic fault creep events in California controlled by shallow frictional heterogeneity. *Nature Geoscience*, 6(7), 566–570. <https://doi.org/10.1038/ngeo1835>
- Wei, M., Sandwell, D., & Fialko, Y. (2009). A silent Mw 4.7 slip event of October 2006 on the Superstition Hills fault, southern California. *Journal of Geophysical Research*, 114, B07402. <https://doi.org/10.1029/2008JB006135>
- Wei, M., Sandwell, D., Fialko, Y., & Bilham, R. (2011). Slip on faults in the Imperial Valley triggered by the 4 April 2010 Mw 7.2 El Mayor-Cucapah earthquake revealed by InSAR. *Geophysical Research Letters*, 38, L01308. <https://doi.org/10.1029/2010GL045235>
- Wei, M., Sandwell, D., & Smith-Konter, B. (2010). Optimal combination of InSAR and GPS for measuring interseismic crustal deformation. *Advances in Space Research*, 46(2), 236–249. <https://doi.org/10.1016/j.asr.2010.03.013>
- Wessel, P., Smith, W. H., Scharroo, R., Luis, J., & Wobbe, F. (2013). Generic mapping tools: Improved version released. *Eos, Transactions American Geophysical Union*, 94(45), 409–410. <https://doi.org/10.1002/2013EO450001>
- Wesson, R. (1988). Dynamics of fault creep. *Journal of Geophysical Research*, 93(B8), 8929–8951. <https://doi.org/10.1029/JB093iB08p08929>
- Williams, P. L., McGill, S. F., Sieh, K. E., Allen, C. R., & Louie, J. N. (1988). Triggered slip along the San Andreas fault after the 8 July 1986 North Palm Springs earthquake. *Bulletin of the Seismological Society of America*, 78(3), 1112–1122.
- Xu, X., Sandwell, D. T., Tymofyeyeva, E., González-Ortega, A., & Tong, X. (2017). Tectonic and anthropogenic deformation at the Cerro Prieto geothermal step-over revealed by Sentinel-1A InSAR. *IEEE Transactions on Geoscience and Remote Sensing*, 55(9), 5284–5292. <https://doi.org/10.1109/TGRS.2017.2704593>
- Xu, X., Tong, X., Sandwell, D. T., Milliner, C. W., Dolan, J. F., Hollingsworth, J., et al. (2016). Refining the shallow slip deficit. *Geophysical Journal International*, 204(3), 1867–1886.



Geophysical Research Letters

Supporting Information for

Surface Creep Rate of the Southern San Andreas Fault Modulated by Stress Perturbations from Nearby Large Events

Xiaohua Xu¹, Lauren Ward², Junle Jiang^{1,3}, Bridget Smith-Konter², Ekaterina Tymofyeyeva¹, Eric O. Lindsey⁴, Arthur G. Sylvester⁵ and David T. Sandwell¹

¹*Institute of Geophysics and Planetary Physics, Scripps Institution of Oceanography, University of California San Diego, La Jolla, CA, USA*

²*Department of Geology and Geophysics, University of Hawaii at Manoa, Honolulu, USA*

³*Department of Earth and Atmospheric Sciences, Cornell University, Ithaca, NY, USA*

⁴*Earth Observatory of Singapore, Nanyang Technological University, Singapore*

⁵*Department of Earth Science, University of California Santa Barbara, Santa Barbara, CA, USA*

Contents of this file

Text S1 to S2

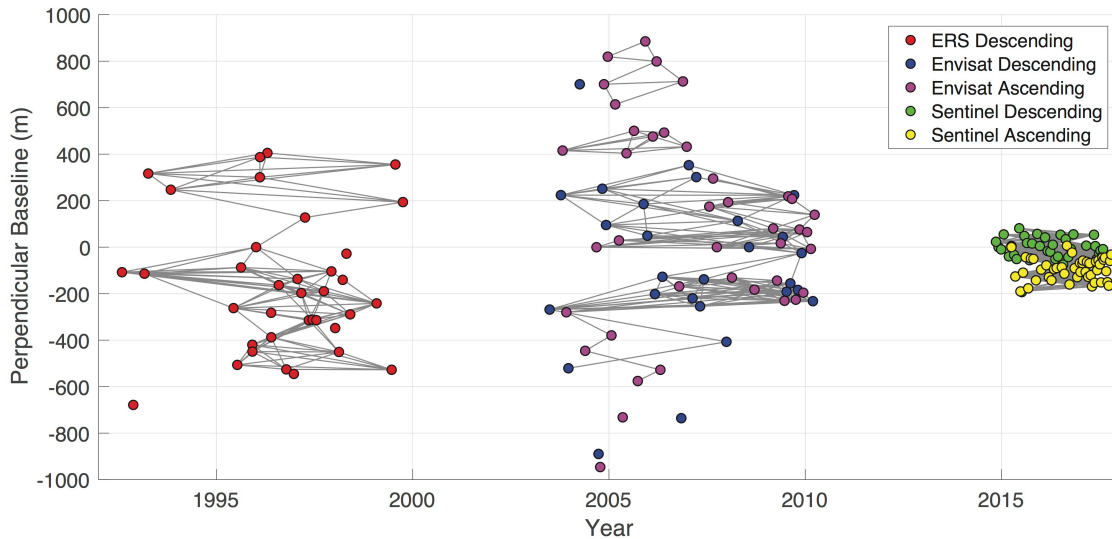
Figures S1 to S10

Text S1. Details of InSAR Data Analysis

We gathered 36 scenes from ERS satellites descending track 356 spanning 08/05/1992 to 06/19/1999 covering the SSAF (Figure 1). We produced 116 interferograms selected based on a 300m perpendicular baseline threshold (Figure S1). For the case of ENVISAT, 28 scenes from descending track 356 spanning 06/28/2003 to 03/13/2010 and 40 scenes from ascending track 77 span 10/27/2003 to 03/29/2010 for this area (Figure 1). We produced 90 interferograms for the descending track and 97 for the ascending track based on 300-m perpendicular baseline threshold (Figure S1). We also processed 38 scenes from Sentinel-1 descending track 173 spanning 11/10/2014 to 08/14/2017 and 46 scenes from Sentinel-1 ascending track 166 spanning 04/03/2015 to 10/19/2017 (Figure 1). The Sentinel-1 dataset we used, compared to other satellite datasets, has a relatively short observation time span and thus a smaller signal-to-atmospheric-noise ratio. However, taking advantage of the Sentinel-1 satellites having a much shorter and regular 12-day

38 cadence, an atmospheric phase correction can be performed before we estimate LOS
 39 velocity with stacking. We first produced 126 and 191 interferograms for the descending
 40 and ascending track based on a 150-m perpendicular baseline and 120-day temporal
 41 baseline threshold. With these short time-span interferograms, we were able to derive
 42 atmospheric phase screens by a common scene stacking approach [Tymofyeyeva and
 43 Fialko, 2015; Xu et al., 2017]. Then we further produced 194 and 190 interferograms for
 44 the descending and ascending track based on a 50-m perpendicular baseline threshold for
 45 any pairs spanning over a year (Figure S1). We subtracted the atmospheric phase screens
 46 from these interferograms and then used stacking methods to obtain the final LOS
 47 velocity map (Figure 2).

48
 49

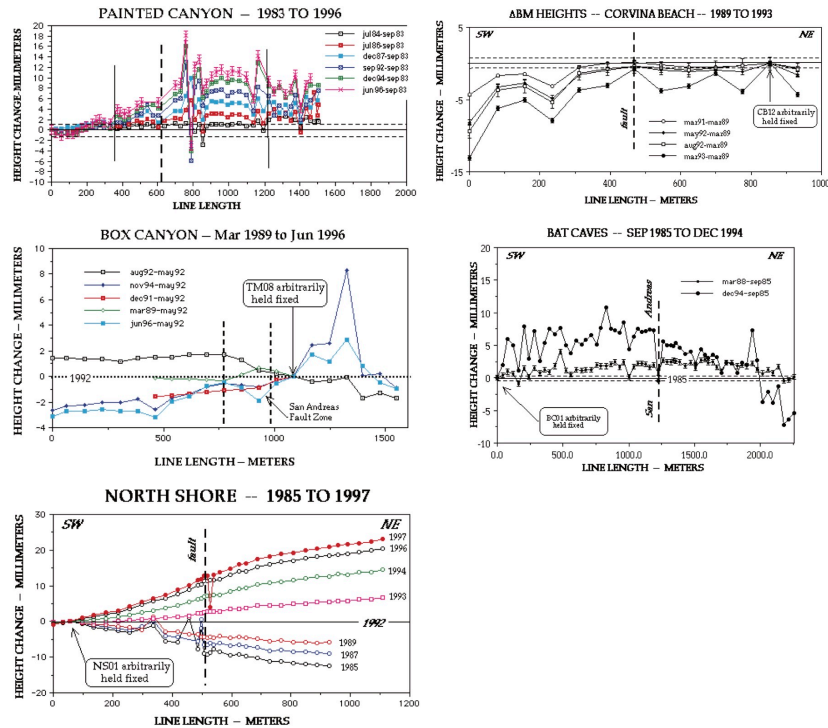


50

51 Figure S1. Perpendicular baseline vs. time plot for the data set used in this study. Each dot
 52 represents a SAR scene with colors denoting different satellites. Each grey line is an
 53 interferogram selected based on the thresholds described in Section 2.

54

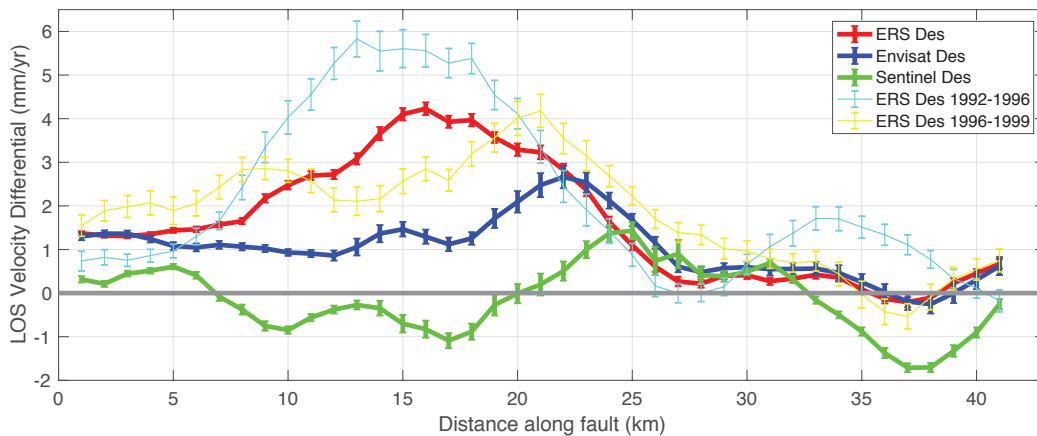
55



56

57 Figure S2. Leveling profiles at the five positions shown in Figure 1. The extracted vertical
 58 velocity for Painted Canyon (PC), Box Canyon (BX), North Shore (NS), Corvina Beach (CV),
 59 and Bat Cave (BC) are 0.60, 0.75, 4.00, -1.00 and -0.75 mm/yr, respectively.

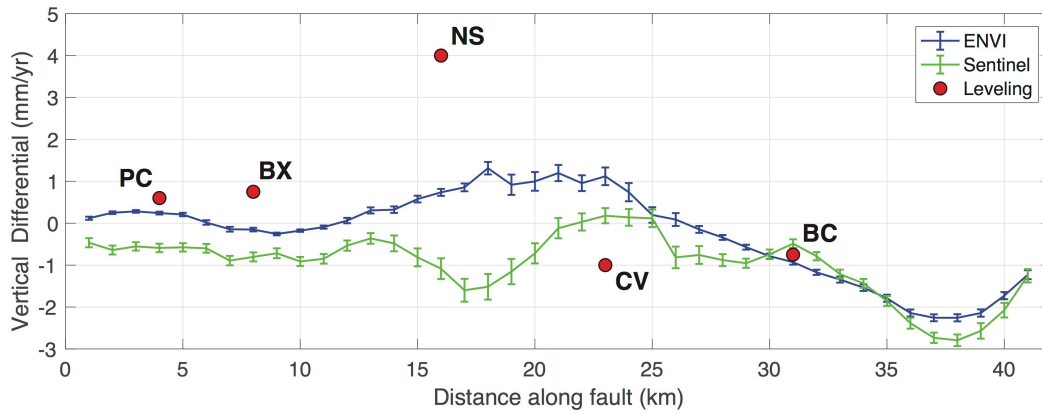
60



61

62 Figure S3. Descending LOS velocity differential along the fault segment. The numbers are
 63 computed by differentiating the intercepts of linear regressions on the data inside 2km by 4km
 64 boxes on each side of the fault.

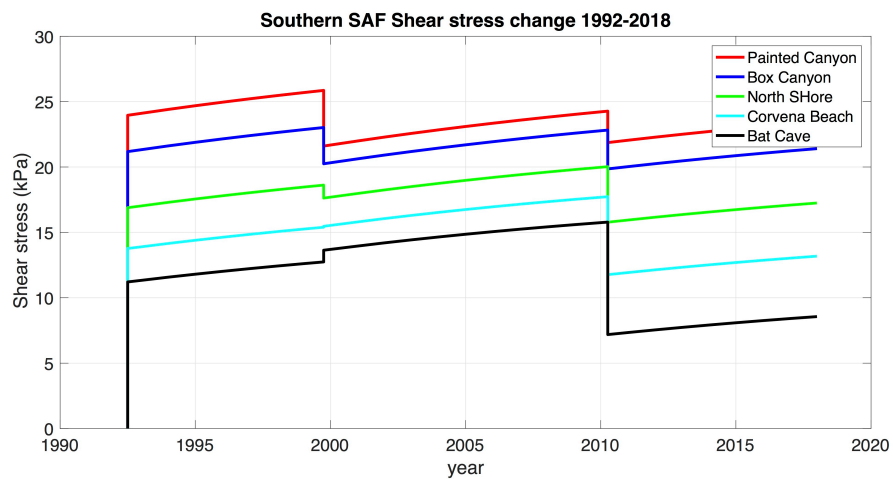
65



66

67 Figure S4. Vertical differentials of the deformation velocity along the fault. The red dots are the
 68 levelling data from Figure S2, corresponding to the ERS time frame. The profiles are the vertical
 69 results from the decomposition with horizontal fault creep plotted in the top panel in Figure 2.

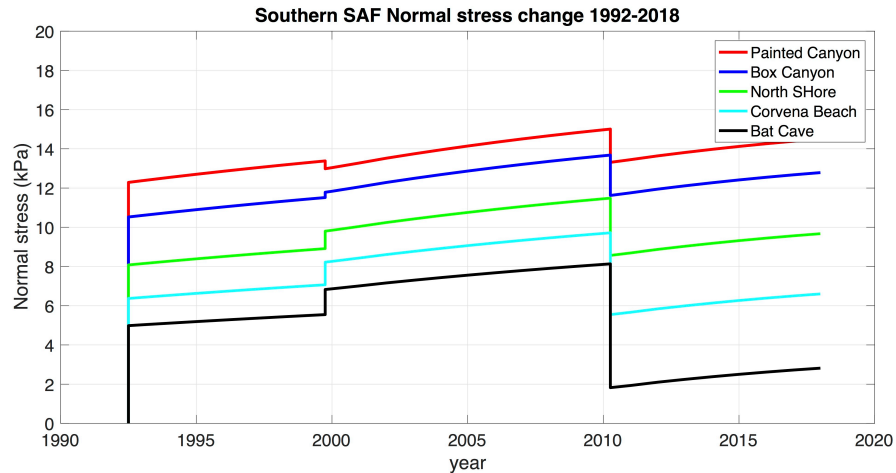
70



71

72 Figure S5. As in Figure 3, coseismic shear stress change and postseismic relaxation along the
 73 SSAF segment (positions provided in Figure 1) in response to the Landers, Hector Mine, and
 74 EMC earthquakes. Interseismic background stressing rates along the SSAF segment and nearby
 75 faults ($\sim 20\text{-}30$ kPa/yr) were omitted for illustrative purposes.

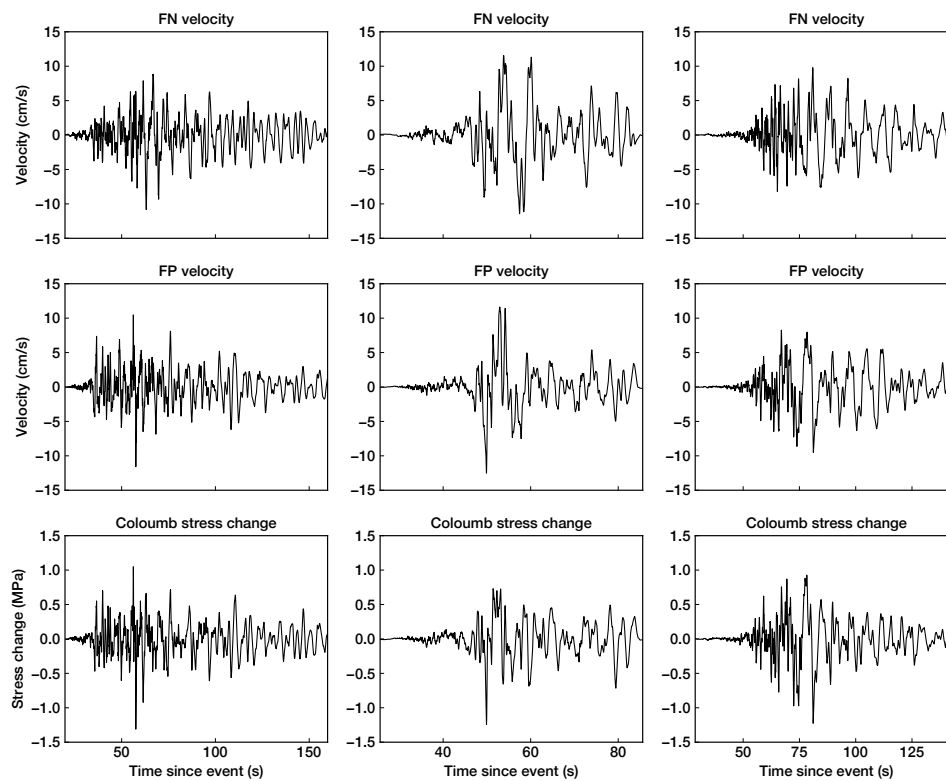
76



77

78 Figure S6. As in Figure 3, coseismic normal stress change and postseismic relaxation along the
 79 SSAF segment (positions provided in Figure 1) in response to the Landers, Hector Mine, and
 80 EMC earthquakes.

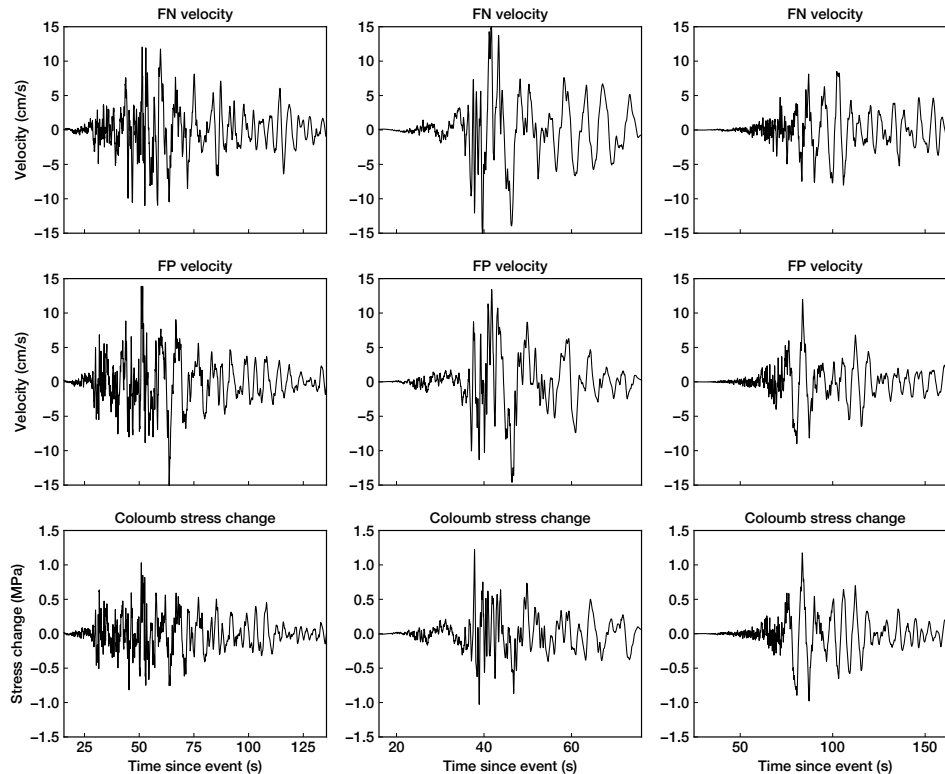
11591



81

82 Figure S7. Coseismic ground motion recorded at the California Geological Survey station 11591
 83 (longitude/latitude: $-115.8298^{\circ}/33.4205^{\circ}$) near Bat Cave and the inferred dynamic stress changes
 84 on the SSAF. (left) Landers, (center) Hector Mine and (right) EMC earthquakes. The particle
 85 velocity in the fault-normal (FN, top) and fault-parallel (FP, middle) directions are shown,

86 assuming a strike angle of 315° . The FN and FP velocities, V , can be approximately related to
 87 dynamic stress perturbations $\Delta\tau$, through $\Delta\tau = \frac{GV}{V_g}$, where G is the rigidity (30 GPa) and V_g is the
 88 group velocity of surface waves (3.5 km/s), and combine into dynamic Coulomb stress changes
 89 (bottom). The velocity seismogram data is downloaded from <https://www.strongmotioncenter.org>.
 90



91

92 Figure S8. Coseismic ground motion recorded at the California Geological Survey station 11625
 93 (longitude/latitude: $-115.9876^\circ/33.5641^\circ$) near Box Canyon and the inferred dynamic stress
 94 changes. Plotting conventions are similar to Figure S7.

95

96 Text S2. 1D rate-and-state fault modeling

97 Here we present results from a 1D spring-slider analog fault model that is governed by
 98 rate-and-state fault friction and with radiation damping. We use this idealized model to
 99 illustrate the typical response of static stress perturbation on fault creep, using model
 100 parameters motivated by the shallow SSAF.

101

102 The force balance equation is as follows:

$$k(V_{pl} \cdot t - \delta) - \tau_f = \frac{\mu}{2c_s} V,$$

103 where k is the stiffness of the spring-slider system, V_{pl} is the long-term plate loading rate
 104 (3 mm/yr), τ_f is the frictional resistance, μ the shear modulus (30 GPa), c_s the shear wave
 105 velocity (3 km/s), and t , V and δ are time, slip rate, and slip, respectively.

106

107 The rate-and-state friction with the slip evolution law [Dieterich, 1979, 1981; Ruina,
 108 1983] is expressed as follows:

$$\tau_f = \sigma f(V, \theta) = \sigma \left[f_o + a \ln \left(\frac{V}{V_o} \right) + b \ln \left(\frac{V\theta}{L} \right) \right];$$

$$\theta = - \frac{V\theta}{L} \ln \left(\frac{V\theta}{L} \right),$$

109 where σ is the effective normal stress, f_o and V_o are the reference coefficient of friction
 110 and reference slip rate, respectively, a and b are the rate-and-state frictional parameters,
 111 and L is the characteristic slip distance.

112

113 We solve these coupled equations, and track the evolution of slip, slip rates, stress, and
 114 state variable of models with velocity-strengthening friction in response to instantaneous
 115 changes in stress τ_f . We consider both positive and negative Coulomb stress changes of
 116 25 kPa, with the amplitude motivated by the Landers case. We choose different values of
 117 model stiffness relative to a characteristic stiffness of the system, namely $k_c = b\sigma/L$
 118 [Perfettini and Ampuero, 2008]. The velocity, displacement, and time in Figure S9 and
 119 S10 are normalized by V_{pl} , L/V_{pl} , and L , respectively.

120

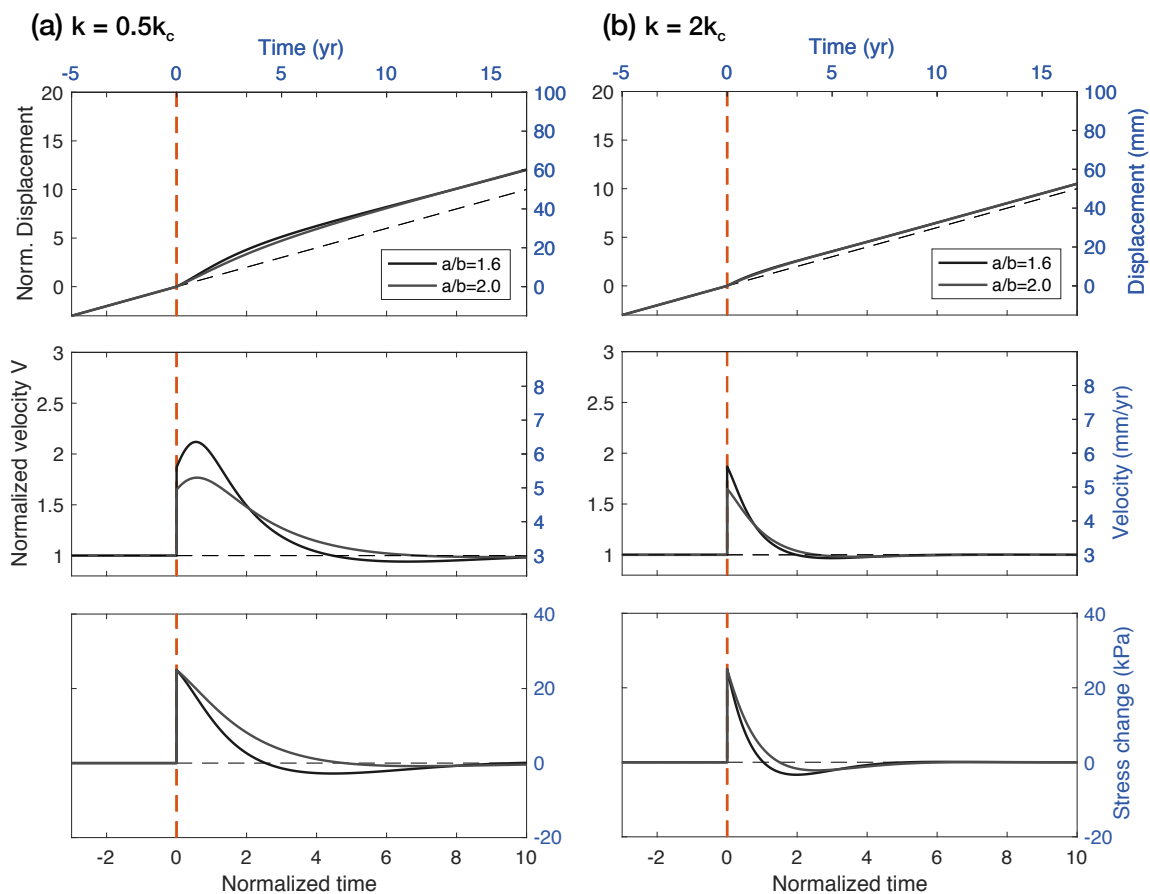
121 The results in Figure S9 and S10 demonstrate that (1) the stress change and the resultant
 122 long-term creep rate are positively correlated and (2) the relaxation time for the post-
 123 perturbation transient is dependent on the system stiffness and rate-and-state parameter L .
 124 The current chosen values of L (5 mm) are larger than laboratory estimates but
 125 comparable to those adopted in seismic cycle simulations that reproduce seismicity and
 126 afterslip with realistic properties [e.g., Lapusta et al., 2000].

127

128 Reference

129 Dieterich, J. H. (1979), Modeling of rock friction .1. Experimental results and constitutive equations, *J.*
 130 *Geophys. Res.*, 84(NB5), 2161-2168, doi:10.1029/JB084iB05p02161.

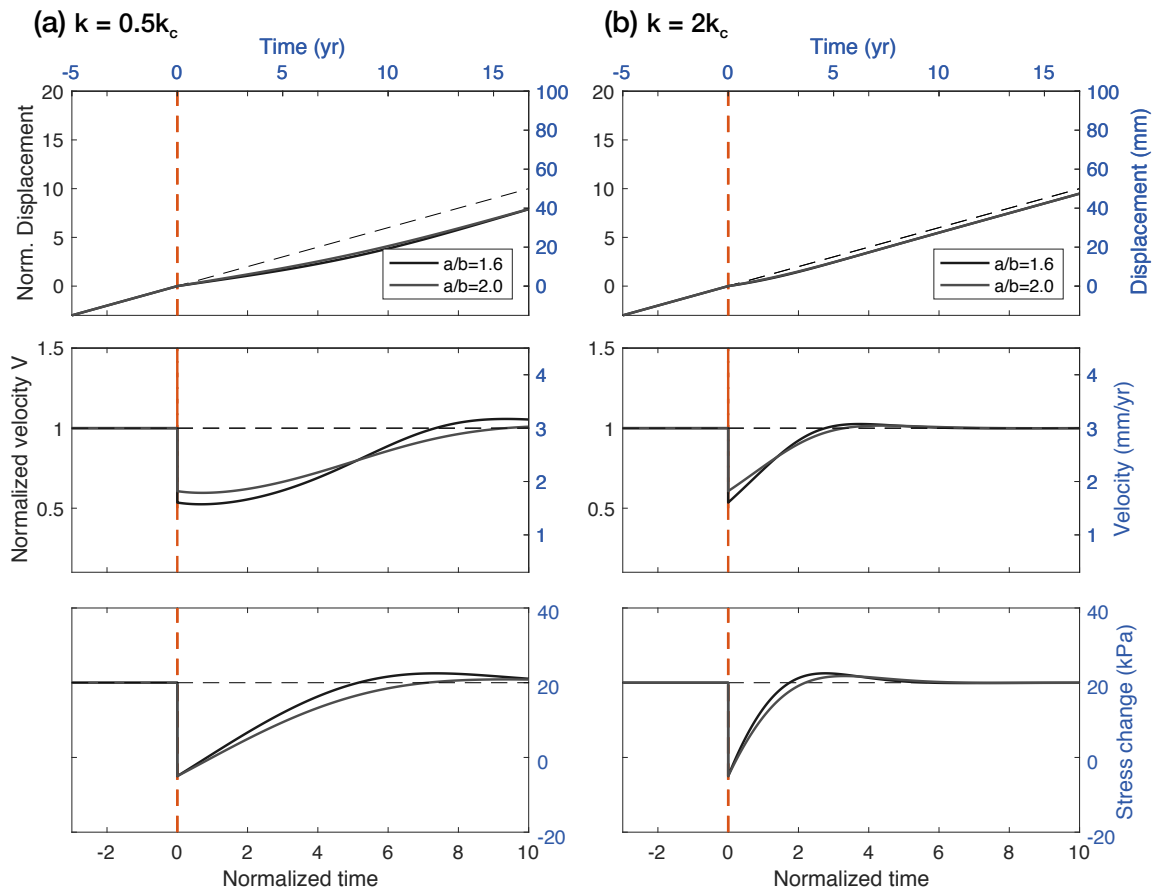
131 Dieterich, J. H. (1981), Potential for geophysical experiments in large scale tests, *Geophys. Res. Lett.*, 8(7),
 132 653-656, doi:10.1029/GL008i007p00653/pdf.
 133 Lapusta, N., Rice, J. R., Ben - Zion, Y., & Zheng, G. (2000). Elastodynamic analysis for slow tectonic
 134 loading with spontaneous rupture episodes on faults with rate - and state - dependent friction. *Journal of*
 135 *Geophysical Research: Solid Earth*, 105(B10), 23765-23789.
 136 Perfettini, H., and J.-P. Ampuero (2008), Dynamics of a velocity strengthening fault region: Implications
 137 for slow earthquakes and postseismic slip, *J. Geophys. Res.*, 113, B09411, doi:10.1029/2007JB005398.
 138 Ruina, A. (1983), Slip instability and state variable friction laws, *J. Geophys. Res. Solid Earth*, 88(B12),
 139 10,359-10,370, doi:10.1029/JB088iB12p10359.
 140



141
 142 Figure S9. The behavior of a velocity-strengthening fault in response to a positive Coulomb stress
 143 change. Models with different system stiffness are shown in (a) $0.5k_c$ and (b) $2k_c$. The evolution
 144 of (top) displacement, (middle) velocity and (bottom) stress are shown for cases of different a/b
 145 ratios (1.6 and 2.0). Other model parameters are: $b=0.001$, $L=5$ mm, $\sigma=20$ MPa, $\Delta\tau=25$ kPa.
 146 Red dashed lines mark the time of the imposed instantaneous stress change. Black dashed lines
 147 indicate the unperturbed model behavior. Note that normalized variables are shown in black and

148 unnormalized variables are shown in blue.

149



150

151 Figure S10. The behavior of a velocity-strengthening fault in response to a negative Coulomb
 152 stress change ($\Delta\tau = -25$ kPa). Plotting conventions are similar to Figure S9.

153

154

155